


RESEARCH ARTICLE

Design and analysis of a climbing robot consisting of a parallel mechanism and a remote center of motion mechanism

Wei Ye¹, Tongwang Huo², Chaoxin Gong² and Zhihong Chen³ 

¹National and Local Joint Engineering Research Center of Reliability Analysis and Testing for Mechanical and Electrical Products, Zhejiang Sci-Tech University, Hangzhou, China

²School of Mechanical Engineering, Zhejiang Sci-Tech University, Hangzhou, China

³China Academy of Aerospace Science and Innovation, Beijing, China

Corresponding author: Zhihong Chen; Email: zhihongch@outlook.com

Received: 19 June 2024; **Revised:** 5 November 2024; **Accepted:** 19 November 2024

Keywords: Climbing robot; parallel mechanism; remote center of motion mechanism; performance evaluation; dimensional optimization

Abstract

This paper presents a climbing robot (CR) designed for the purpose of pipeline maintenance, with capability to avoid the risks inherent in manual operations. In the design process, a three degree of freedom (DOF) parallel mechanism coupled with a remote center of motion (RCM) mechanism linkage mechanism were designed to serve as the CR's climbing mechanism, which met the specific demands for climbing movements. The modified Kutzbach–Grübler formula and the screw theory were applied to calculate the DOFs of the CR. Then, the inverse and forward position analysis for the CR was derived. Furthermore, velocity and acceleration analysis of parallel mechanism were conducted and derived the Jacobian matrix, through which the singularity of parallel mechanism was analyzed. In order to evaluate kinematic performance of parallel mechanism, the motion/force transmission index (LTI) of workspace was calculated, which directed the followed dimensional optimization process. According to the optimization result, a prototype was constructed and a series of motion experiments were carried out to validate its climbing capability.

1. Introduction

As urban development and construction continue to progress, an increasing number of tall cylindrical poles, such as utility poles, streetlights, and billboards, emerge within city. With the continual expansion of cities, tasks related to the inspection, repair, and cleaning of these structures have become more complex and challenging. Traditional manual operation not only consumes time and labor but also poses safety risks, with higher expenses.

To overcome these limitations and enhance operational efficiency, climbing robots (CRs) [1–5] have become a viable solution. These robots are able to move on external surfaces of pipelines or walls and can perform tasks including inspection, maintenance, and cleaning. Based on their motion mechanism structures, CRs can be broadly categorized into four types: the first type is the wheeled type, for example, Ahmadabadi M N et al. [6–9] developed a hoop-type wheeled CR University of Tehran-Pole Climbing Robot (UT-PCR), which utilized three wheels to encircle the pipe to generate frictional force. The second type uses serial mechanism structures for movement, these CRs exhibit high flexibility and large workspace. For example, Kushihashi et al. [10, 11] developed the WOODY-1 with a serial robotic arm structure, which was utilized to transport logging workers to the workspace. The third type is parallel type, which uses the parallel mechanism for movement. For example, Saltaren R et al. [12, 13] proposed a CR with a motion system based on a six degrees of freedom (DOFs) Stewart–Gough parallel platform.

Table I. Comparison of different types of climbing robots.

Performance	Wheeled type	Serial type	Parallel type	Hybrid type
Climbing speed	Fast	Slow	Fast	Average
Ability to cross obstacles	Poor	Better	Average	Average
Load capacity	Average	Poor	Better	Average
Structure compactness	Average	Better	Average	Average

The fourth is hybrid type, which uses a combination of series and parallel mechanisms for movement, for example, Tavakoli et al. [14–16] developed a four DOFs CR that combined a 3-RRR (R denotes a revolute joint) robotic arm with a rotating axis device, enabling it to cross obstacles on the pipeline.

In practical applications, the CRs discussed earlier have certain limitations. To elaborate, wheeled CRs [17–19] need to maintain contact between wheels and pipelines, resulting in an inability to cross obstacles. Serial CRs [20–25] exhibit weak terminal bearing capacity and overall rigidity due to their serial mechanical structures. Parallel CRs [26] have disadvantages of redundant DOF, complex control, and small workspace. Most of the above CRs lack the DOF to rotate around the axis of pipe, which is significant for CRs to cross obstacles. The characteristics of the above types of CRs are summarized in Table I.

Considering the limitations of existing CRs, this paper presents a novel CR that incorporates a combination of parallel mechanisms and remote center of motion (RCM) linkage mechanisms as climbing mechanism. Compared with above CRs, this CR has several advantages, including good load-bearing capacity, no redundant DOF, and the capability of obstacle crossing. Remainder of the paper is arranged as follows: Section 2 analyzes the minimum DOF required for climbing movement and determines the configuration of the CR. In Section 3, the closed-loop vector approach is employed for position analysis, followed by a numerical search to calculate the CR’s workspace. Velocity and singularity analyses are executed using screw theory. In Section 4, the performance analysis and dimensional optimization are carried out. In Section 5, a prototype is designed and constructed based on the optimization results, followed by the execution of several foundational experiments to validate CR’s climbing capability. Section 6 provides a conclusion to the study.

2. Problem formulation

The existing CRs have limitations in terms of complex structure, excessive weight, and inadequate flexibility, etc. In this research, the main objective is to develop a compact CR that possesses good load capacity and obstacle crossing ability. To achieve this goal, we will propose a new type of CR that combines a parallel mechanism and a RCM linkage. The parallel part executes the main function of climb, while the RCM linkage allows the rotational motion around the target object. Performance analysis and dimensional optimization will be carried out to ensure that the CR has good performance. Prototype will be fabricated on which primary experiments are carried out, which verify the feasibility of the proposed CR.

In this research, the members in the mechanism are treated as rigid bodies, that is, their elastic deformations during motion are not considered. Moreover, the gaps in joints are also neglected. In summary, all the analyses including kinematics, performance, optimization, and simulation, etc., are based on above assumptions, which significantly reduces the analysis complexity and is reasonable in primary design stage.

3. Design of the CR

In order to determine the configuration of CR, it is essential to analyze the climbing environments. Cross-interface pipeline environment is relatively common, and if a CR can climb smoothly in such

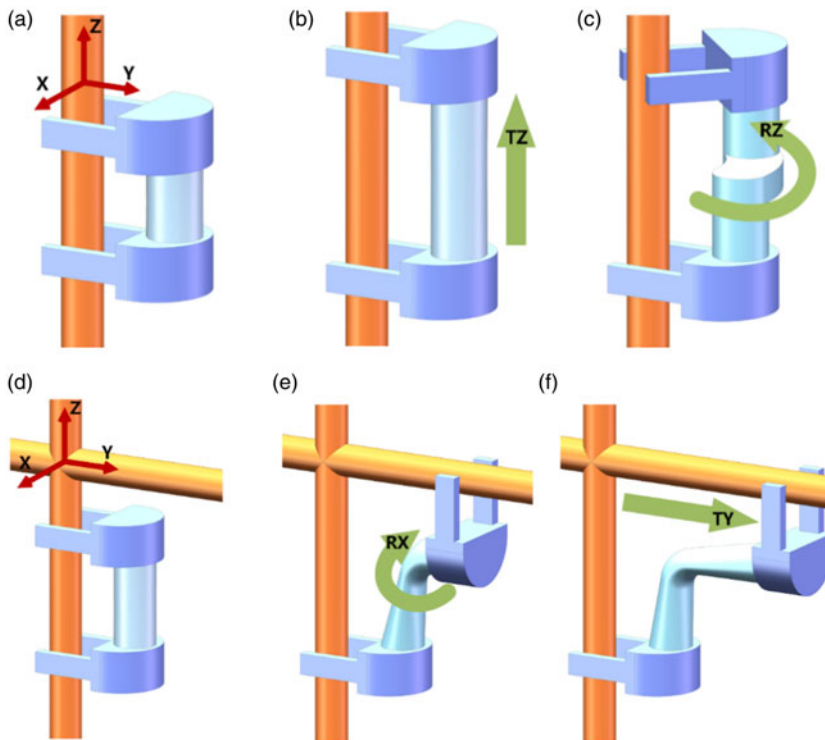


Figure 1. The minimum DOF required for climbing motion: (a) climbing environment 1; (b) TZ climbing DOF; (c) RZ climbing DOF; (d) climbing environment 2; (e) RX climbing DOF; and (f) TY climbing DOF.

environment, it can likely adapt to most other climbing environments. The most fundamental DOFs required for climbing cross-interface pipeline are the axial movement along the pipeline, denoted as DOF TZ, as shown in Figure 1(b). To cross interface, the robot requires radial rotation and translational DOFs along the pipeline, specifically the RX and TY, as shown in Figure 1(e), (f). These three DOFs are adequate for crossing through two-dimensional cross-type pipelines.

By adding an additional DOF for pipe axial rotation, denoted as RZ and as shown in Figure 1(c), climbing capability of CR can be extended into three-dimensional space. This enhancement endows the CR with the capability to cross obstacles. Such an expansion not only broadens CR's workspace but also enhances adapt capability and effectiveness when facing complex pipeline structures.

Using parallel CR with four DOFs mentioned above can address the issue of redundant DOFs inherent to parallel CRs, and it can avoid the drawbacks of poor load-bearing in serial CRs and inability of crossing obstacles in wheeled CRs. However, after extensive research, no suitable parallel mechanisms with such four DOFs were found. Therefore, this paper proposes breaking down the four DOFs required into two part and introduces a novel hybrid CR. The structure of the CR is shown in Figure 2, and the 3-RPR parallel mechanism provides the TZ, TY, RX, and RCM linkage mechanism that supplies the RZ component.

The CR is composed in the following order: the upper gripping mechanism, the parallel mechanism, the RCM linkage mechanism, and the lower gripping mechanism as shown in Figure 2. The gripper mechanisms have centering and positioning functions. In the process of climbing movement, one of the grippers will grip the pipe to provide positioning function. The axis Z of the RCM linkage and parallel mechanisms is collinear with the center axis of the upper and lower gripper mechanisms, respectively, which ensures that the CR's rotational DOF RZ coincides with the axis of the pipe.

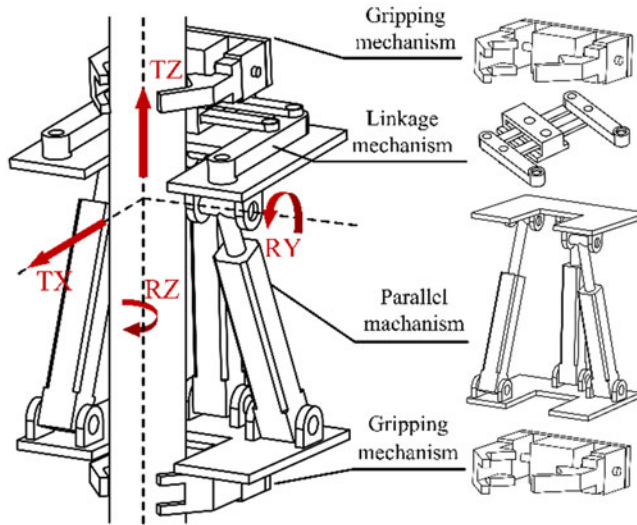


Figure 2. The structure of CR.

As shown in Figure 3, the parallel mechanism is a 3-RPR mechanism composed of three identical RPR limbs connecting the upper and lower platforms. The centers of the R joints connected to the upper platform are denoted as P_1 , P_2 , and P_3 , and the centers of the R joints connected to the lower platform are denoted as B_1 , B_2 , and B_3 . All R joints on the upper platform are parallel and axis of P_2 is denoted as y axis, and all R joints on the lower platform are parallel and axis of B_1 is denoted as Y axis. To eliminate singularities, axis B_2 is located between axes B_1 and B_3 , while axis P_1 is located between axes P_2 and P_3 . The distance from the rotational joint P_1 to the axis y is denoted as L_4 , while the distance from the rotational joint B_2 to axis Y is denoted as L_3 . P_3 is located at the midpoint of the perpendicular bisector of the line segment between the projection of point P_1 onto the axis of y and point P_2 , while B_3 is located at the midpoint of the perpendicular bisector of the line segment between the projection of point B_2 onto the axis of Y and point B_1 . The projection of points P_1 , P_2 and B_1 , B_2 onto the x -axis is 2D apart. The distance from P_3 to the axis y is denoted as L_2 , while the distance from B_3 to the axis Y is denoted as L_1 . Using the midpoint of the line connecting the projection of point P_1 onto the axis y and point P_2 as the origin, a coordinate system O_2 - xyz is established, where the axis y is along the direction of the P_2 axis, the axis x is parallel to the axis of R joint, and the axis z is determined according to the right-hand rule. The coordinate system O_1 - XYZ is set up in the same way as the coordinate system O_2 - xyz .

The motion screw system of limb i expressed in the global coordinate system is given as:

$$\begin{aligned} \mathcal{S}_{i1} &= [\mathbf{y}^T \quad \mathbf{b}_i \times \mathbf{y}^T]^T \\ \mathcal{S}_{i2} &= [0^T \quad \mathbf{b}_i \mathbf{p}_i]^T \\ \mathcal{S}_{i3} &= [\mathbf{y}^T \quad \mathbf{p}_i \times \mathbf{y}^T]^T \end{aligned} \quad (1)$$

where \mathbf{p}_i is the position vector of P_i , \mathbf{b}_i is the position vector of B_i , and \mathbf{y} is the unit vector along axis u . Then, three reciprocal motion screws of limb i can be yielded as:

$$\begin{aligned} \mathcal{S}_1^C &= [0 \quad 0 \quad 0 \quad 1 \quad 0 \quad 0]^T \\ \mathcal{S}_2^C &= [0 \quad 0 \quad 0 \quad 0 \quad 0 \quad 1]^T \\ \mathcal{S}_3^C &= [0 \quad 1 \quad 0 \quad 0 \quad 0 \quad 0]^T \end{aligned} \quad (2)$$

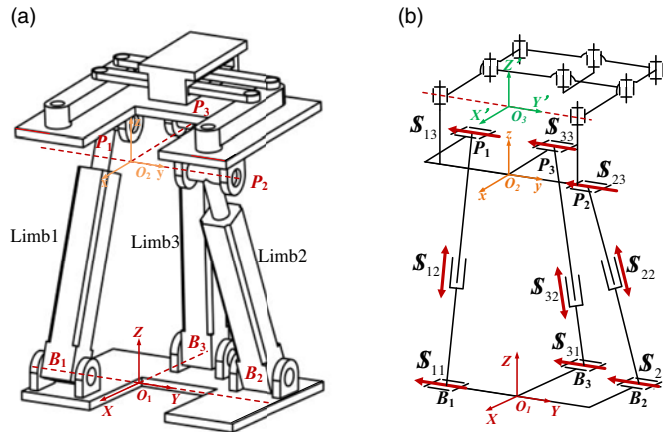


Figure 3. Motion mechanism structure of CR: (a) main motion structure of CR and (b) schematic diagram.

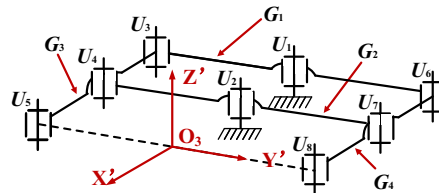


Figure 4. Schematic diagram of the linkage mechanism.

According to the screw theory, the reverse screw of the motion screw in the parallel mechanism corresponds to the constraint screw:

$$\begin{aligned} \mathcal{S}_1^{\omega} &= [0 \ 0 \ 0 \ 0 \ 1 \ 0]^T \\ \mathcal{S}_2^{\omega} &= [0 \ 0 \ 1 \ 0 \ 0 \ 0]^T \\ \mathcal{S}_3^{\omega} &= [1 \ 0 \ 0 \ 0 \ 0 \ 0]^T \end{aligned} \quad (3)$$

The three motion screws represent the motions that the parallel mechanism can achieve under the constraints of the constraint screws. Therefore, the parallel mechanism has three DOFs, rotation around the axis Y , and translation along the axis X and Z .

The remote center linkage mechanism is a type of parallelogram linkage mechanism, as shown in Figure 4. In the links G_1 and G_2 , R joints at both ends of links are utilized to connect the links G_3 and G_4 , while R joints in middle of links are utilized to connect the gripping mechanism. In the links G_3 and G_4 , two R joints are utilized to connect link G_1 and G_2 , while one R joint connected to the platform of the parallel mechanism. All rotational joint axes are parallel to the z -axis direction of the lower platform coordinate system O_2-xyz . The coordinate system $O_3-X'Y'Z'$ was established by copying the O_2-xyz coordinate system vertically down to the plane of the RCM linkage mechanism.

Then, according to the modified Kutzbach–Grübler formula the DOF of RCM linkage mechanism was calculated:

$$M = d(n - g - 1) + \sum_{i=1}^g f_i + v \quad (4)$$

Given the order of mechanism $d = 3$, the number of linkage $n = 6$, the number of the moving pairs $g = 8$, and the redundancy constraints $v = 2$, the DOF M is equal to 1. By integrating the parallel

Table II. Motion mechanism structure dimensional parameters.

Symbol/Unit	Geometric meaning of parameters
L_1/mm	Distance from B_3 to B_1
L_2/mm	Distance from P_3 to P_2
L_3/mm	Distance from B_2 to B_1
L_4/mm	Distance from P_1 to P_2
D/mm	Distance from B_1, B_2 along axis Y
hz	Distance from O_2 to O_3
q_i/mm	Linear distance along the B_iP_i line ($i = 1 \sim 3$)
q_4/mm	Rotation distance of rods 1 and 2 about their central axes
x, z	Relative position vector of the claw center
α/rad	Rotation angle of the upper platform around the axis Y
β/rad	Rotation angle of the upper platform around the axis Z

mechanism with RCM linkage mechanism, the CR's main motion mechanism is formed. The motion mechanism possesses two rotational and two translational DOFs.

4. Kinematic analysis

4.1. Inverse position modeling

A position analysis is conducted to determine the relationship between the relative position of the CR's gripper centre and the actuator inputs. First, the dimensional parameters of the CR are provided in Table II.

Expressing the position vectors of point B_i ($i = 1, 2, 3$) in the global coordinate system as:

$$\begin{cases} \mathbf{r}_{b1} = [0 & -D & 0]^T \\ \mathbf{r}_{b2} = [-L_1 & D & 0]^T \\ \mathbf{r}_{b3} = [-L_3 & 0 & 0]^T \end{cases} \quad (5)$$

Similarly, position vectors of point P_i ($i = 1, 2, 3$) expressed in the local coordinate system can be written as:

$$\begin{cases} \mathbf{r}_{p1}^{cs2} = [-L_4 & -D & 0]^T \\ \mathbf{r}_{p2}^{cs2} = [0 & D & 0]^T \\ \mathbf{r}_{p3}^{cs2} = [-L_2 & 0 & 0]^T \end{cases} \quad (6)$$

A constraint equation can be established for limb i as:

$$\begin{cases} |\mathbf{r}_{p1} - \mathbf{r}_{b1}| = q_1 \\ |\mathbf{r}_{p2} - \mathbf{r}_{b2}| = q_2 \\ |\mathbf{r}_{p3} - \mathbf{r}_{b3}| = q_3 \end{cases} \quad (7)$$

Now, through the closed-loop vector method, combined with the above equations, the inverse solution for the position can be obtained as:

$$\begin{cases} q_1 = \sqrt{(D \cos \beta - D + L_4 \cos \alpha \sin \beta)^2 + (z - hz + L_4 \sin \alpha)^2 + (x + D \sin \beta - L_4 \cos \alpha \cos \beta)^2} \\ q_2 = \sqrt{(D - D \cos \beta)^2 + (x - D \sin \beta + L_1)^2 + (z - hz)^2} \\ q_3 = \sqrt{(L_2 \cos \alpha \sin \beta)^2 + (x - L_2 \cos \alpha \cos \beta + L_3)^2 + (z - hz + L_2 \sin \alpha)^2} \end{cases} \quad (8)$$

4.2. Forward position modeling

Forward kinematics involves using a set of actuation variables (q_1, q_2, q_3) as inputs to solve the position and orientation parameters (x, z, α) of the moving platform. Based on Eq. (8), we have

$$\begin{cases} (x + A_1)^2 + A_2^2 + (z + A_3)^2 - q_1^2 = 0 \\ (x + C_1)^2 + (z - hz)^2 + C_2^2 - q_2^2 = 0 \\ D_1^2 + (x + D_2)^2 + (z + D_3)^2 - q_3^2 = 0 \end{cases} \quad (9)$$

in which

$$\begin{aligned} A_1 &= D \sin \beta - L_4 \cos \alpha \cos \beta; A_2 = D \cos \beta - D + L_4 \cos \alpha \sin \beta; A_3 = L_4 \sin \alpha - hz; \\ C_1 &= L_1 - D \sin \beta; C_2 = D - D \cos \beta; D_1 = L_2 \cos \alpha \sin \beta; D_2 = L_3 - L_2 \cos \alpha \cos \beta; D_3 = L_2 \sin \alpha - hz \end{aligned}$$

Eq. (9) can be rewritten in the following forms as:

$$\begin{cases} x^2 + z^2 + 2A_1x + 2A_3z + E_1 = 0 \\ x^2 + z^2 + 2C_1x - 2hz \cdot z + E_2 = 0 \\ x^2 + z^2 + 2D_2x + 2D_3z + E_3 = 0 \end{cases} \quad (10)$$

where

$$E_1 = A_1^2 + A_2^2 + A_3^2 - q_1^2; E_2 = C_1^2 + C_2^2 + hz^2 - q_2^2; E_3 = D_1^2 + D_2^2 + D_3^2 - q_3^2$$

In Eq. (10), subtracting the first equation from the second, and the first from the third, respectively, we have

$$\begin{cases} 2(A_1 - C_1)x + 2(A_3 + hz)z + E_1 - E_2 = 0 \\ 2(A_1 - D_2)x + 2(A_3 - D_3)z + E_1 - E_3 = 0 \end{cases} \quad (11)$$

Expressions of x and z can be obtained as:

$$\begin{cases} x = \frac{\delta_1}{\delta} \\ z = \frac{\delta_2}{\delta} \end{cases} \quad (12)$$

where

$$\begin{aligned} \delta &= 2[(A_1 - C_1)(A_3 - D_3) - (A_1 - D_2)(A_3 + hz)]; \delta_1 = (E_1 - E_2)(D_3 - A_3) + (E_1 - E_3)(A_3 + hz); \\ \delta_2 &= (E_1 - E_2)(A_1 - D_2) + (E_1 - E_3)(A_1 - C_1) \end{aligned}$$

Substituting Eq. (12) into the first equation of Eq. (10) yields

$$\delta_1^2 + \delta_2^2 + 2A_1\delta\delta_1 + 2A_3\delta\delta_2 + E_1\delta^2 = 0 \quad (13)$$

Eq. (13) contains only one unknown parameters α . It is actually a 12th-degree polynomial, through which α can be calculated. Substituting the solution of α into Eq. (12), the final solutions for x and z can be obtained, and the direct position analysis is finished.

4.3. Workspace analysis

The reachable workspace of the CR refers to the positions that the gripping mechanism can reach. The structural parameters of the mechanism are given as follows: $L_1 = 100$ mm, $L_2 = 100$ mm, $L_3 = 75$ mm, $L_4 = 75$ mm, driving range $q_1/q_2/q_3 = 120 \sim 240$ mm, and $q_4 = -45^\circ \sim 45^\circ$, and the rotational range of the joints is $-30^\circ \sim 30^\circ$.

Based on the inverse kinematics, using numerical search method, the orientation workspace and translational workspace are calculated and shown in Figures 5 and 6.

The orientation workspace is the orientation positions that parallel mechanism can reach [27], and overall workspace of the mechanism is formed by the RCM linkage mechanism and the parallel

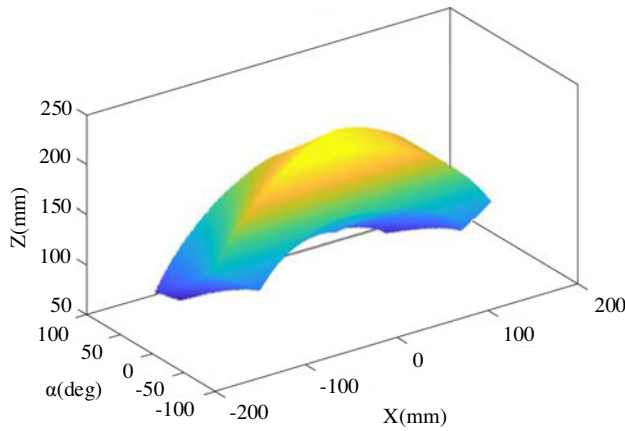


Figure 5. Orientation workspace of the PM.

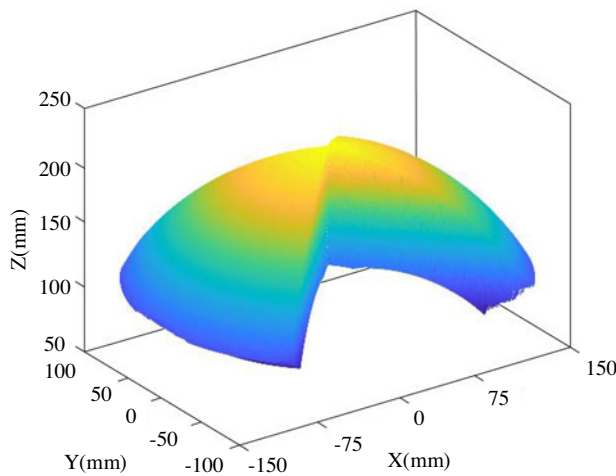


Figure 6. Translational workspace of the PM.

mechanism. The CR may have both upper and lower platforms as moving platforms during operation. However, the workspace is corresponding one-to-one, with only a modification in the reference coordinate; therefore, it is no need to further illustrated.

4.4. Velocity analysis

Based on the screw theory, velocity analysis of the mechanism is performed. By locking all branches except for the screw corresponding to the driving joint, a new set of constraint screw systems is obtained. This screw system compared to the original screw system has an additional screw, which is the transmission force screw of the driving joint. Then, transmission force screws of each branch can be represented as follows:

$$\begin{cases} \mathcal{S}_{T1} = [\mathbf{r}_{p1b1} & \mathbf{r}_{b1} \times \mathbf{r}_{p1b1}] \\ \mathcal{S}_{T2} = [\mathbf{r}_{p2b2} & \mathbf{r}_{b2} \times \mathbf{r}_{p2b2}] \\ \mathcal{S}_{T3} = [\mathbf{r}_{p3b3} & \mathbf{r}_{b3} \times \mathbf{r}_{p3b3}] \end{cases} \quad (14)$$

According to the screw theory, the linear combination of the motion screws of the branches is equivalent to the motion screw of the moving platform. Then, the motion screw of the moving platform is

represented as:

$$\begin{aligned}\mathcal{S}_p &= [\omega_p^T \quad v_p^T]^T \\ \mathcal{S}_p &= \omega_{i1}\mathcal{S}_{i1} + \omega_{i2}\mathcal{S}_{i2} + \omega_{i3}\mathcal{S}_{i3}\end{aligned}\quad (15)$$

where \mathcal{S}_p is the motion screw of the moving platform with respect to the reference at the origin of the upper platform. v_p^T and w_p^T represent the linear velocity and angular velocity vectors of the platform in the global coordinate system. The w_{ij} represents the motion quantity of the j -th joint on the i -th branch. The reciprocal product of the transmission screw is performed on both sides of Eq. (15):

$$\begin{aligned}\mathcal{S}_{T1} \circ \mathcal{S}_p &= \omega_{12}\mathcal{S}_{T1} \circ \mathcal{S}_{12} \\ \mathcal{S}_{T2} \circ \mathcal{S}_p &= \omega_{22}\mathcal{S}_{T1} \circ \mathcal{S}_{22} \\ \mathcal{S}_{T3} \circ \mathcal{S}_p &= \omega_{32}\mathcal{S}_{T1} \circ \mathcal{S}_{32}\end{aligned}\quad (16)$$

By representing the above equation with a matrix, it can be concluded that

$$J_T \mathcal{S}_p = J_q \dot{q} \quad (17)$$

The matrixes J_T and J_q can be express as follows:

$$J_T = \begin{bmatrix} \mathcal{S}_{T1} \\ \mathcal{S}_{T2} \\ \mathcal{S}_{T3} \end{bmatrix} \quad J_q = \begin{bmatrix} \mathcal{S}_{T1} \circ \mathcal{S}_{11} & 0 & 0 \\ 0 & \mathcal{S}_{T2} \circ \mathcal{S}_{21} & 0 \\ 0 & 0 & \mathcal{S}_{T1} \circ \mathcal{S}_{31} \end{bmatrix} \quad \dot{q} = \begin{bmatrix} \dot{q}_1 \\ \dot{q}_2 \\ \dot{q}_3 \end{bmatrix} \quad (18)$$

Moving the J_q term to other side of the Eq. (17) and substituting the expression for the branch velocity screw, the relationship between the branch joint velocity and the drive joint velocity was obtained:

$$\omega_i = (J_T^{-1} J_q J_i)^{-1} \dot{d} = G_i \dot{q} \quad (19)$$

where G_i is called the first-order influence coefficient matrix [28] of branch i :

$$G_i = \begin{bmatrix} G_{\omega i1}^1 & G_{\omega i1}^2 & G_{\omega i1}^3 \\ G_{\omega i2}^1 & G_{\omega i2}^2 & G_{\omega i2}^3 \\ G_{\omega i3}^1 & G_{\omega i3}^2 & G_{\omega i3}^3 \end{bmatrix} \quad (20)$$

The motion screw of the j -th joint of the i -th branch can be expressed by the above equation combined with the drive joint velocities:

$$\mathcal{S}_{ij} = [\omega_{ij}^T \quad v_{ij}^T]^T = \mathcal{S}_{ij}^1 \dot{q}_1 + \mathcal{S}_{ij}^2 \dot{q}_2 + \mathcal{S}_{ij}^3 \dot{q}_3 \quad (21)$$

where \mathcal{S}_{ij}^k represents the assisting motion screw of the k -th drive on the j -th joint of the i -th branch:

$$\mathcal{S}_{ij}^k = G_{\omega i1}^k \mathcal{S}_{i1}^1 + \dots + G_{\omega ij}^k \mathcal{S}_{ij}^j \quad (22)$$

4.5. Acceleration analysis

Based on the velocity analysis, the acceleration screw A_o of the moving platform can be expressed as:

$$A_o = \dot{\omega}_{i1}\mathcal{S}_{i1} + \dot{\omega}_{i2}\mathcal{S}_{i2} + \dots + \dot{\omega}_{ij}\mathcal{S}_{ij} + \mathcal{S}_{Li} \quad (i = 1, 2, 3) \quad (23)$$

where

$$\mathcal{S}_{Li} = (\dot{\omega}_{i1}\mathcal{S}_{i1}) \circ (\dot{\omega}_{i2}\mathcal{S}_{i2} + \dots + \dot{\omega}_{ij}\mathcal{S}_{ij}) + (\dot{\omega}_{i2}\mathcal{S}_{i2}) \circ (\dot{\omega}_{i3}\mathcal{S}_{i3} + \dots + \dot{\omega}_{ij}\mathcal{S}_{ij}) + \dots + (\dot{\omega}_{ij-1}\mathcal{S}_{ij-1}) \circ (\dot{\omega}_{ij}\mathcal{S}_{ij}) \quad (24)$$

The acceleration for the joints in i -th branch is given by:

$$\dot{\omega}_i = J_i^{-1} (A_o - \mathcal{S}_{Li}) \quad (25)$$

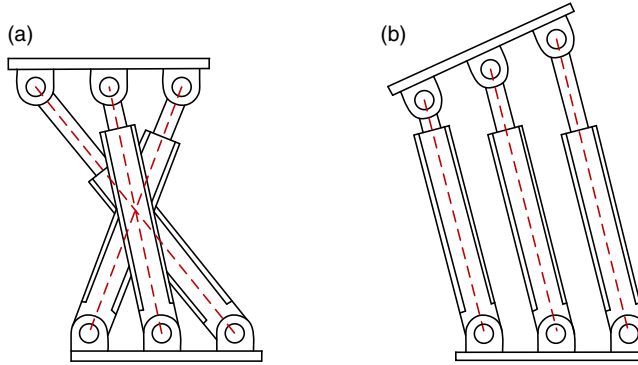


Figure 7. Singular configurations: (a) singular configuration 1 and (b) singular configuration 2.

Therefore, the acceleration screw of the j -th joint in i -th branch is

$$\mathbf{A}_{ij} = \begin{bmatrix} \dot{\boldsymbol{\omega}}_{ij}^T & (\mathbf{a}_{ij} - \boldsymbol{\omega}_{ij} \times \mathbf{v}_{ij})^T \end{bmatrix}^T \quad (26)$$

4.6. Singularity analysis

When the parallel mechanism moves to a specific configuration, its DOF may differ from the theoretically calculated DOF and the motion characteristics of the mechanism change. Such configurations are referred to as singular configurations.

The occurrence of singularities can be found by examining the rank of matrices in Eq. (17). When the rank of \mathbf{J}_T is reduced, inverse kinematic singularity occurs, and when the rank of \mathbf{J}_q is reduced rank matrix, a forward kinematic singularity occurs. If both matrices have reduced ranks, a mixed singularity occurs.

Considering the mutual orthogonality between the motion screw and the transmission force screw, neither inverse kinematic singularities nor mixed singularities will occur. According to the screw theory [29–31] and Grassmann line geometry theory [32–34], the rank decreases in two specific cases. The first case is when transmission force screws intersect at one point, as shown in Figure 7(a). The second case is when transmission force screws are parallel, which results in a rank deficiency, as shown in Figure 7(b), and leading to forward kinematic singularity. During the movement of the robot, it is necessary to try to stay away from these two postures.

To visually show the singularities, numerical search method is used here, which yields the singular surface of this parallel mechanism as in Figure 8.

4.7. Simulation

In order to verify the correctness of the kinematic modeling, simulations will be carried out in this part. Without loss of generality, the motion trajectory of the upper platform is defined as:

$$\begin{cases} \alpha = \frac{\pi}{180} \left(27 \frac{t^5}{10000} - 27 \frac{t^4}{400} + 9 \frac{t^3}{80} \right) \\ \beta = \frac{\pi}{180} \left(9 \frac{t^5}{10000} - 9 \frac{t^4}{400} + 3 \frac{t^3}{20} \right) \\ x = \left(9 \frac{t^5}{2500} - 9 \frac{t^4}{100} + 3 \frac{t^3}{5} \right) + 20 \\ z = \left(21 \frac{t^5}{2500} - 21 \frac{t^4}{100} + 7 \frac{t^3}{5} \right) + 200 \end{cases} \quad (t = 0 \sim 10s) \quad (27)$$

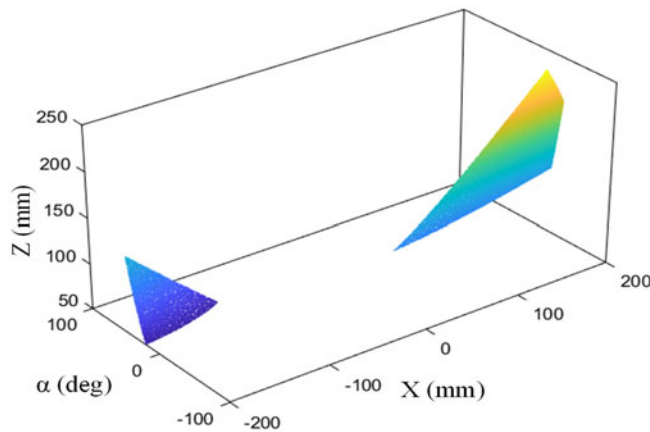


Figure 8. Singular surface.

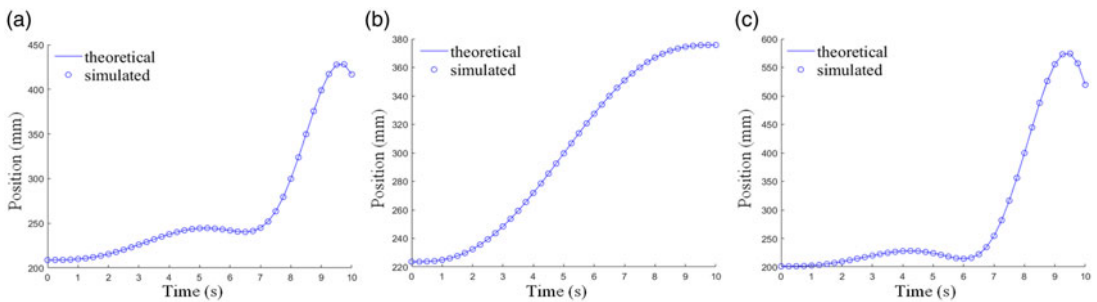


Figure 9. Comparison of theoretical and simulated results of position analysis: (a) drive joint 1; (b) drive joint 2; and (c) drive joint 3.

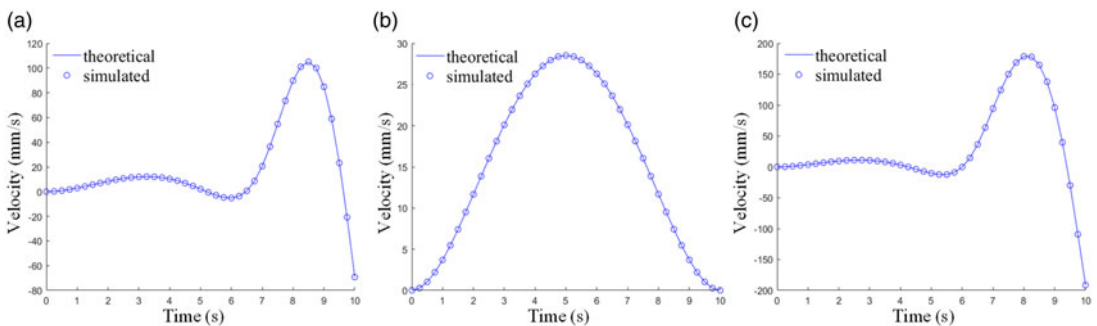


Figure 10. Comparison of the theoretical and simulated results of the velocity analysis: (a) drive joint 1; (b) drive joint 2; and (c) drive joint 3.

The simulation results about inverse position, velocity, and acceleration are represented by circles in Figures 9, 10, and 11, respectively. In comparison, the theoretical results are represented by solid lines. It can be found the simulation results match well with the theoretical results, which verifies the kinematics analysis.

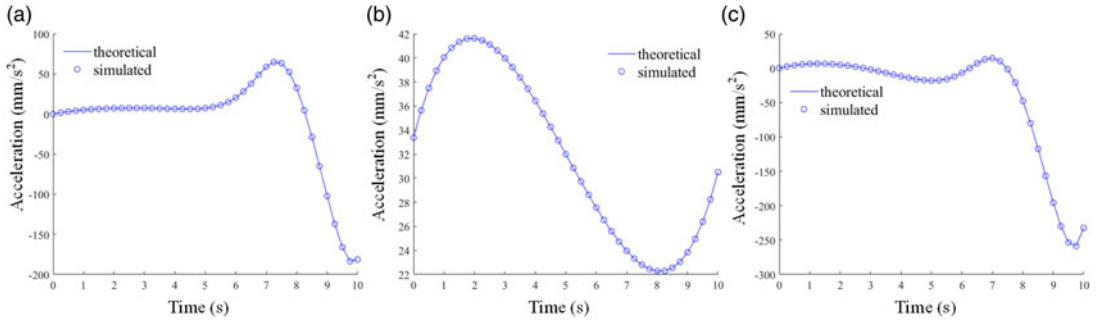


Figure 11. Comparison of the theoretical and simulated results of the acceleration analysis: (a) drive joint 1; (b) drive joint 2; and (c) drive joint 3.

5. Performance analysis and optimization

5.1. Kinematic performance evaluation

In order to evaluate the kinematic performance of the CR, it is necessary to conduct a performance evaluation. There are many indexes for performance evaluation, including kinematic, stiffness, and dynamic indices that can be utilized to measure the performance of parallel mechanisms. Among various performance indices, the motion/force transmission index [35–38] is independent with reference and dimensionless, which belongs to the category of kinematic performance that will be utilized here.

The LTI includes three indexes: input transmission index (ITI), output transmission index (OTI), and local transmission index (LTI), and the physical significance of these indexes is the instantaneous power of the actuating force in the direction of motion. The larger the index, the higher the instantaneous power and the superior kinematic performance. In order to evaluate the ITI of the input end, the i -th branch input transmission performance index is defined as:

$$\lambda_i = \min \left\{ \frac{|\mathcal{S}_{Ti} \circ \mathcal{S}_{fi}|}{|\mathcal{S}_{Ti} \circ \mathcal{S}_{fi}|_{\max}} \right\} \quad (28)$$

where \mathcal{S}_{Ti} represents the force transmission screw corresponding to the driving joint on the i -th branch and \mathcal{S}_{fi} represents the motion screw corresponding to the driving joint on the branch i . Then, the definition of OTI is as follows:

$$\eta = \min \left\{ \frac{|\mathcal{S}_{Ti} \circ \mathcal{S}_{oi}|}{|\mathcal{S}_{Ti} \circ \mathcal{S}_{oi}|_{\max}} \right\} \quad (29)$$

where \mathcal{S}_{oi} is the output motion screw corresponding to the driving force screw \mathcal{S}_{Ti} , which refers to the motion screw of platform when all other driving joints are locked. Once the ITI and OTI of the parallel mechanism are obtained, in order to evaluate the overall transmission performance, LTI is introduced and calculated as following Eq. (29):

$$\Gamma = \min \{ \lambda_i \quad \eta_i \} \quad (30)$$

The range of values for the LTI is 0 to 1, which is independent of coordinate systems and dimensions. Based on the defined indexes, the distribution of the LTI for the 3-RPR parallel mechanism is shown in Figure 12(b). To facilitate the observation of the distribution of LTI values throughout the entire workspace, the workspace is discretized into multiple planes at the angle θ values. The distribution of LTI values on these planes is illustrated in Figure 12(a).

Each plane in Figure 12(a) represents the LTI in the workspace of the parallel mechanism for different α values, which can be utilized for subsequent dimensional optimization based on LTI. It can be observed that the workspace changes with the variations of α .

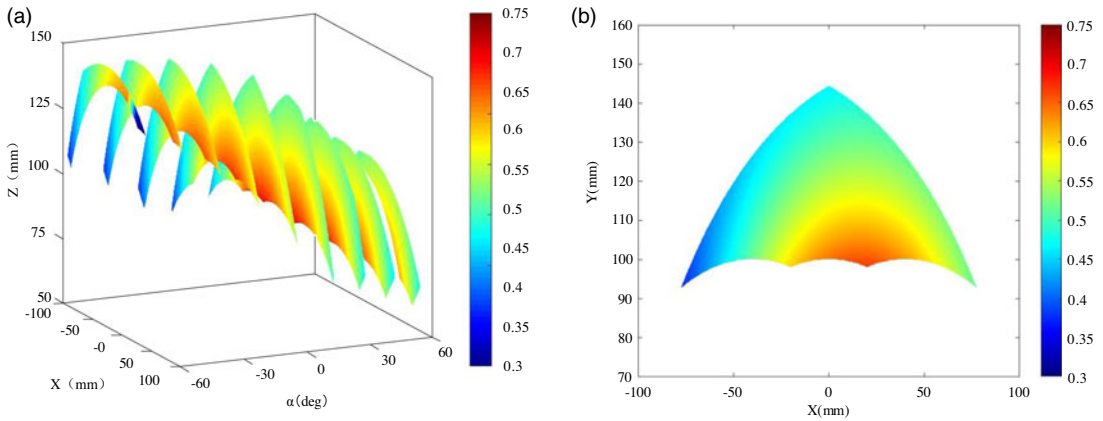


Figure 12. LTI distribution of CR: (a) in three dimensional workspace and (b) in prescribe workspace with $\alpha = 0^\circ$.

For the CR, both the upper and lower platforms along with their coordinates can serve as the fix platform and reference coordinate system. Thus, their LTI in that coordinate system need to be considered. However, the LTI is independent of the coordinate system and depend only on the parallel mechanism's configuration. Therefore, whether the lower platform or the upper platform coordinate system is utilized as the reference, the calculated LTI results of will be the same, and there is no need to repeat the calculation of LTI.

5.2. Dimensional optimization

Based on the LTI in the previous section, the Performance Chart-based Design Methodology [39–42] (PCbDM) can be utilized to optimize the dimension with LTI as the optimization target. To further reduce the number of parameters, the Parameter Finiteness Normalization Method (PFNM) is utilized, considering L_1 , L_2 , L_3 , and L_4 as the characteristic parameters of the parallel mechanism:

$$L_2 = kL_1 \quad k = (0 \sim 1) \quad (31)$$

Let the normalized parameters is set as:

$$r_i = L_i/D_i = (1, 2, 3) \quad r_4 = 1 - (r_1 + r_2 + r_3) \quad (32)$$

The constraints condition is set as:

$$\begin{cases} r_1 \geq r_3 \\ r_2 \geq r_4 \\ r_1 \geq r_2 \end{cases} \quad (33)$$

Equations (32) and (33) together with these conditions define a three-dimensional space, which is referred to as the Parameter Design Space (PDS) and is illustrated in Figure 13.

If the value of k is fixed, the PDS becomes a plane that is cut by a plane perpendicular to r_1 and r_2 within the cube. When $k = 1$, $r_1 = r_2$, and the PDS is shown in Figure 14(a). The three-dimensional PDS can then be visualized as a two-dimensional image, as shown in Figure 14(b).

After PFNM, a series of similar mechanisms can be obtained through different proportion coefficients D . These mechanisms exhibit similarity in specific indexes, such as LTI, and are referred to as similarity mechanisms (SMs). By calculating the performance of a mechanism, its performance as well as the performance of SM can be obtained. Therefore, PCbDM can simplify the optimization process and improve optimization efficiency.

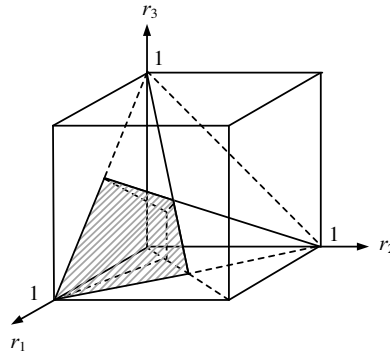


Figure 13. PDS of the CR.

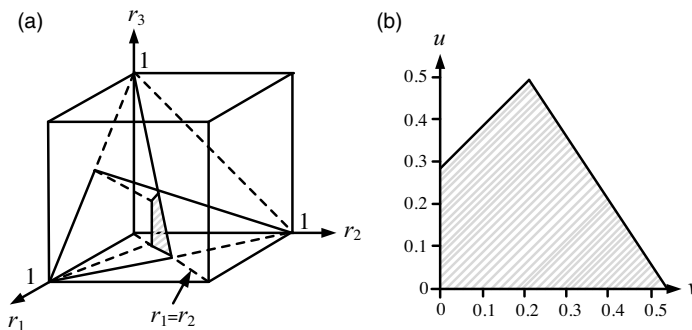


Figure 14. Two-dimensional image of PDS: (a) PDS in three dimension space and (b) PDS in two-dimensional space.

The above proposed LTI reflects only the kinematic performance of the mechanism in a single configuration. In order to evaluate the overall performance of the workspace, let the $\Gamma \geq 0.5$ region be defined as high-quality kinematic space. Subsequently, the global transmission index (GTI) is set as:

$$\sigma_t = \frac{\int_{S_G} dW_s}{\int_S dW_s} \quad (34)$$

where W_s represents the given workspace of the mechanism and S_G represents the area of high-quality kinematic space. The range of GTI values is 0~1, where the larger value indicates the better kinematic performance of the CR.

Since LTI does constant regardless of the reference coordinate system, it only needs to be optimized and calculated once. Optimized images are obtained for various values k values, and the best optimal result image was obtained when $k = 1$, as illustrated in Figure 15.

After comprehensively considering the optimization result, the chosen optimized result is $L_1 : L_2 : L_3 : L_4 = 1 : 1 : 0.75 : 0.65$. To verify the efficiency of the optimization, the LTI distribution graph for both the optimized and the original mechanism were created and the result was shown in Figure 16.

From the optimization results, it can be seen that after optimization, the performance of the mechanism has been optimized and the workspace range has also increased. These improvements proved the effectiveness of the optimization.

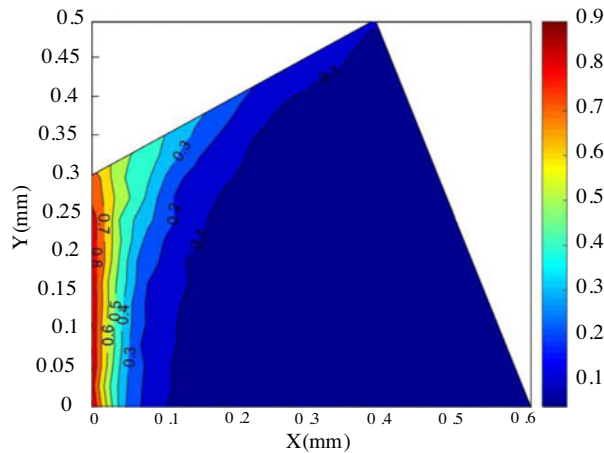


Figure 15. GTI distribution map.

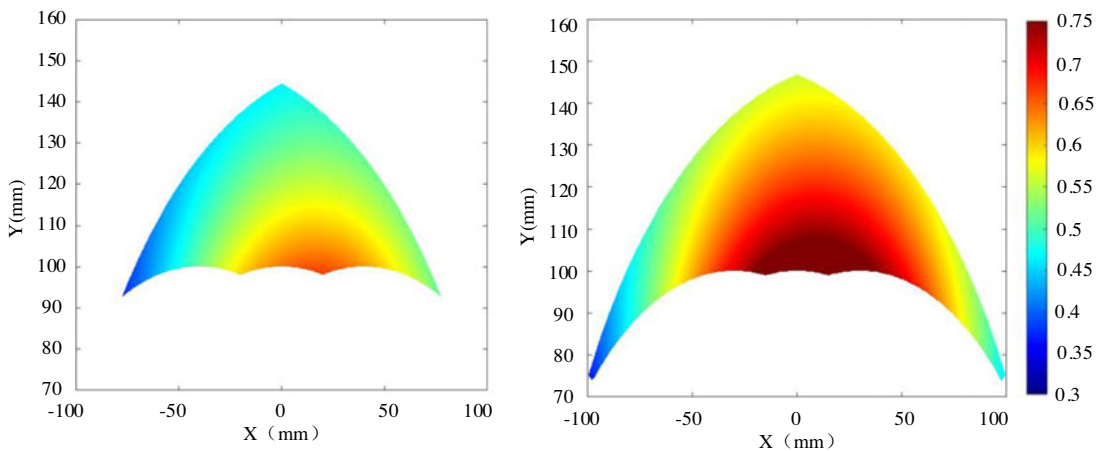


Figure 16. LTI distribution before and after optimization.

6. Prototype design and experimentation

According to the optimized characteristic parameters obtained in the previous section, a prototype was designed and built, as shown in Figure 17.

As shown in Figure 17, the prototype's actuation consists of three electric cylinders (LA150-032D), an electric cylinder drive board (AET-LA-85), three bus servos (HTS-20L), a servo drive board (DPS-0313), and a computer. The parallel mechanism is driven by the electric cylinder acting as R joint and controlled by both drive board and computer. Each electric cylinder has a mass of 110 g, a stroke length of 50 mm, and a maximum speed of 17 mm/s and can withstand a maximum force of 50 N. The RCM linkage mechanism is driven by the bus servos, with a rotation range of $\pm 30^\circ$, which is controlled by the corresponding drive board and computer. The gripper mechanism is also controlled by a bus motor, with a maximum torque of 0.20 N.m. Theoretically, it can generate a maximum clamping force of 40 N, and the driving method is the same as the linkage mechanism. The total mass of the prototype is approximately 2 kg.

To study the kinematic performance of the CR, several climbing motion experiments were conducted, and the results are shown in Figures 18, 19, and 20. It can be observed that the prototype climbs 50 mm in each straight climb, and it takes 5 s to complete one straight climb task. Therefore, the climbing speed of the CR is about 8.33 mm/s. The robot's capability to rotate around the pipe axis was also verified,

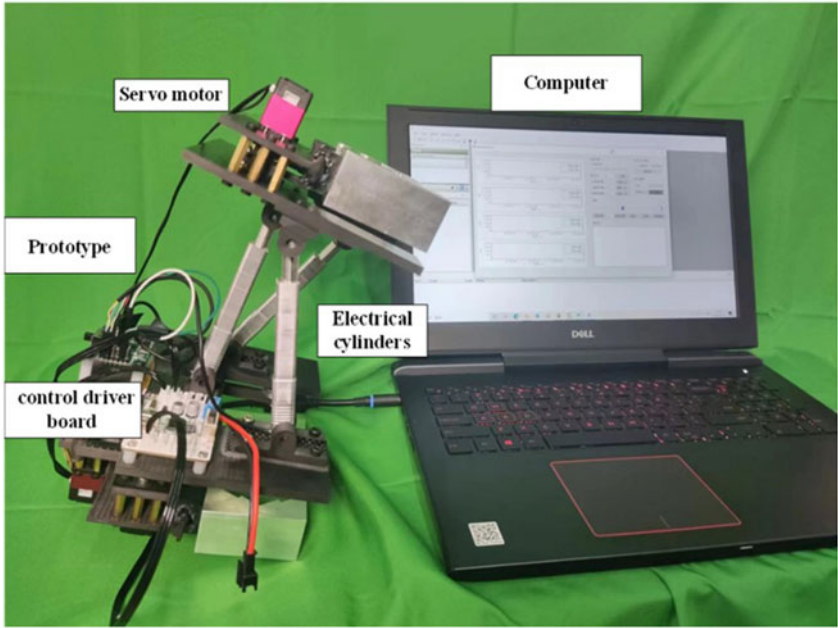


Figure 17. CR prototype.

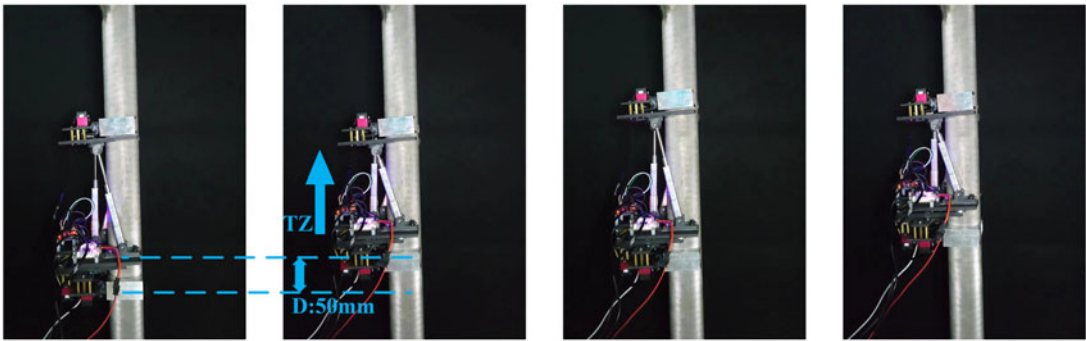


Figure 18. Experiment of straight line climbing.

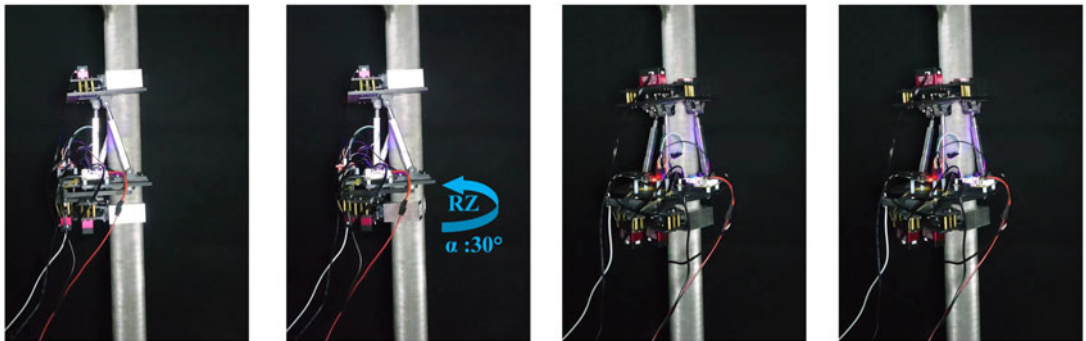


Figure 19. Experiment of move around the pipe.

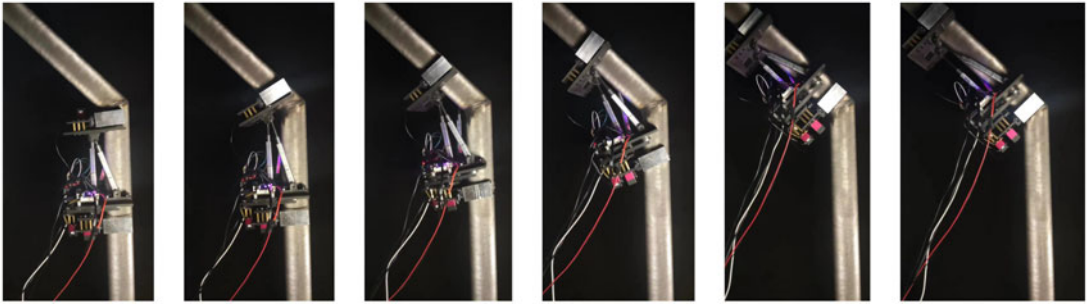


Figure 20. Experiment of climbing curved pipe.

as shown in Figure 19, with the rotation range of 30° per movement. Finally, to validate the motion capability of the CR, a climbing experiment on a curved pipe was conducted, as shown in Figure 20, and the CR smoothly completed the climbing experiment. From the above experimental research, it is verified that the CR has at least four DOFs and its climbing capability.

7. Conclusion

This paper proposes a four DOFs CR which combines a parallel mechanism and RCM linkage mechanism as the motion mechanism. First, the required DOFs for climbing movement were analyzed, and the configuration of the CR was determined. Subsequently, kinematic analysis of the mechanism was conducted, which included analyses of DOF, velocity, acceleration, and workspace. Then, focused on the CR's performance, the LTI was calculated, and performance distribution charts were plotted. Based on the goal of improving the LTI, the mechanism's dimension was optimized using the PCbDM method. Finally, a prototype was designed and built according to the optimization results, and several climbing experiments were conducted to validate the motion performance of the mechanism. The prototype is composed of simple mechanical and driving components, and future improvements can be made to enhance its kinematic performance for practical applications.

Author contributions. Wei Ye, Tongwang Huo, and Zhihong Chen conceived and designed the study, Chaoxin Gong underwent an experimental setup, and Zhihong Chen did a text proofreading.

Financial support. The work is supported by the National Natural Science Foundation of China (NSFC) under Grant No. 52375033 and the Natural Science Foundation of Zhejiang Province under Grant No. ZCLZ24E0501.

Competing interests. The author(s) declare(s) that there are no conflicts of interest of this paper.

Ethical approval. None.

References

- [1] J. C. Grieco, M. Prieto, M. Armad and P. Gonzalez de Santos, "A six-legged climbing robot for high payloads," *In: Proceedings of the 1998 IEEE International Conference on Control Applications (Cat No 98CH36104)*, IEEE (1998), pp. 446–450.
- [2] A. Jalal, R. Kant, A. Kumar and V. Kumar, "Pipe climbing robot," (2022), arXiv preprint arXiv: [2201.07865](https://arxiv.org/abs/2201.07865).
- [3] J.-H. Kim, J.-C. Lee and Y.-R. Choi, "PiROB: vision-based pipe-climbing robot for spray-pipe inspection in nuclear plants," *Int. J. Adv. Robot. Syst.* **15**(6), 1729881418817974 (2018).
- [4] A. Saunders, D. I. Goldman, R. J. Full and M. Buehler, "The rise climbing robot: Body and leg design," *In: Unmanned Systems Technology VIII* (SPIE, 2006) pp. 401–413.

- [5] M. Minor, H. Dulimarta, G. Danghi, R. Mukherjee, R. Lal Tummala and D. Aslam, "Design, implementation, and evaluation of an under-actuated miniature biped climbing robot," *In: Proceedings 2000 IEEE/RSJ International Conference on Intelligent Robots and Systems (IROS 2000) (Cat No 00CH37113)* (IEEE, 2000) pp. 1999–2005.
- [6] A. Baghani, M. N. Ahmadi and A. Harati, "Kinematics modeling of a wheel-based pole climbing robot (UT-PCR)," *In: Proceedings of the 2005 IEEE international Conference on Robotics and Automation* (IEEE, 2005) pp. 2099–2104.
- [7] M. N. Ahmadi, H. Moradi, A. Sadeghi, A. Madani and M. Farahnak, "The evolution of UT pole climbing robots," *In: 1st International Conference on Applied Robotics for the Power Industry* (IEEE, 2010) pp. 1–6.
- [8] H. Hosseini, H. Najafi, M. Mehrabadi, B. Gholamian, S. Noroozi, M. Ahmadi, Z. Ziafati Kafi, N. Sadri, A. Hojabr Rajeoni and A. Ghalyanchilangeroudi, "Molecular detection of fowl adenovirus 7 from slaughtered broiler chickens in Iran: The first report," *Iran. J. Vet. Res.* **22**(3), 244–247 (2021).
- [9] C. Yuan, Y. Chang, Y. Song, S. Lin and F. Jing, "Design and analysis of a negative pressure wall-climbing robot with an omnidirectional characteristic for cylindrical wall," *Robotica*, **42**(7), 2226–2242 (2024).
- [10] Y. Kushihashi, K. Yoshikawa, K. Imai, A. Terashima and Y. Miwa, "Development of Tree Climbing and Pruning Robot, Woody-1," *In: Proc JSME Conf on Robotics and Mechatronics* (Tokyo, 2006).
- [11] H. Kawasaki, S. Murakami, H. Kachi and S. Ueki, "Novel climbing method of pruning robot," *In: 2008 SICE Annual Conference* (IEEE, 2008) pp. 160–163.
- [12] R. Saltaren, R. Aracil, O. Reinoso and M. A. Scarano, "Climbing parallel robot: A computational and experimental study of its performance around structural nodes," *IEEE Trans. Robot.* **21**(6), 1056–1066 (2005).
- [13] R. Saltarén, R. Aracil, J. Sabater, O. Reinoso and L. M. Jimenez, "Modelling, Simulation and Conception of Parallel Climbing Robots for Construction and Service," *In: 2nd Int Workshop & Conf on CLIMBING & WALKING ROBOTS (CLAWAR)* (1999).
- [14] M. Tavakoli, L. Marques and A. T. Almeida, "Self calibration of step-by-step based climbing robots," *In: 2009 IEEE/RSJ International Conference on Intelligent Robots and Systems* (IEEE, 2009) pp. 3297–3303.
- [15] M. Tavakoli, L. Marques and A. T. De Almeida, "A low-cost approach for self-calibration of climbing robots," *Robotica* **29**(1), 23–34 (2011).
- [16] M. Tavakoli, P. Lopes, L. Sgrigna and C. Viegas, "Motion control of an omnidirectional climbing robot based on dead reckoning method," *Mechatronics* **30**, 94–106 (2015).
- [17] H. Eto and H. Asada, "Development of a wheeled wall-climbing robot with a shape-adaptive magnetic adhesion mechanism," *In: 2020 IEEE International Conference on Robotics and Automation (ICRA)* (IEEE, 2020) pp. 9329–9335.
- [18] M. Lauria, Y. Pigué and R. Siegrwart, "Octopus: an autonomous wheeled climbing robot," *In: Proceedings of the Fifth International Conference on Climbing and Walking Robots (CLAWAR'02)* (2002) pp. 315–322.
- [19] E. Noohi, S. S. Mahdavi, A. Baghani and M. N. Ahmadi, "Wheel-based climbing robot: Modeling and control," *Adv. Robot.* **24**(8-9), 1313–1343 (2010).
- [20] L. Jiang, Y. Guan, X. Zhou, X. Zhang and H. Zhang, "Grasping analysis for a biped climbing robot," *In: IEEE International Conference on Robotics and Biomimetics* (IEEE, 2010) pp. 579–584.
- [21] Y. Guan, L. Jiang, H.C. Zhu, X. Zhou, C. Cai and W. Wu, "A modular bio-inspired biped climbing robot," *In: 2011 IEEE/RSJ International Conference on Intelligent Robots and Systems* (IEEE, 2011) pp. 1473–1478.
- [22] Y. Guan, L. Jiang, X. Zhang and H. Zhang, "Climbing gaits of a modular biped climbing robot," *In: IEEE/ASME International Conference on Advanced Intelligent Mechatronics* (IEEE, 2009) pp. 532–537.
- [23] S. Hong, M. A. Pei-Sun and W. Guang-Rong, "An inchworm locomotion gait based on serpenoid curve for snakelike robot," *Mach. Design Res.* (2008) **24**(1):39–4150.
- [24] H. Shukui, W. Bin and D. Ren, "Design and motion of a redundant snake robot," *In: International Conference on Measuring Technology & Mechatronics Automation, Changsha, China*, (IEEE, 2010), vol. 1, pp. 962–965.
- [25] S. Hong, M. Peisun and W. Guangrong, "Inchworm locomotion gait for snakelike robot," *J. Southeast Univ.* **23**(4), 556–560 (2007).
- [26] M. Wilson, J. M. Sabater, R. J. Saltarén, R. Aracil, E. Yime and J. M. Azorín, "Teleoperated parallel climbing robots in nuclear installations," *Ind. Robot Int. J.* **33**(5), 381–386 (2006).
- [27] D. Pacheco Quiñones, D. Maffiodo and A. Laribi, "Kinematic analysis, workspace definition, and self-collision avoidance of a quasi-spherical parallel manipulator," *Robotica*, 1–26 (2024).
- [28] Z. Huang, Q. Li and H. Ding, *Theory of Parallel Mechanisms*, vol. 6 (Springer, Dordrecht Heidelberg New York London, 2013).
- [29] E. Minguzzi, "A geometrical introduction to screw theory," *Eur. J. Phys.* **34**(3), 613–632 (2013).
- [30] R. S. Ball, "The theory of screws: A study in the dynamics of a rigid body," *Math. Ann.* **9**(4), 541–553 (1876).
- [31] J. K. Davidson, K. H. Hunt and G. R. Pennock, "Robots and screw theory: Applications of kinematics and statics to robotics," *J. Mech. Des.* **126**(4), 763–764 (2004).
- [32] D. Fearnley-Sander, "Hermann Grassmann and the creation of linear algebra," *Am. Math. Monthly* **86**(10), 809–817 (1979).
- [33] J.-P. Merlet, "Singular configurations of parallel manipulators and Grassmann geometry," *Int. J. Robot. Res.* **8**(5), 45–56 (1989).
- [34] J. Wei, B. Yu, C. Liu, J. Song, J. Zhang and C. Meng, "Grassmann line geometry based configuration synthesis of equivalent Uu parallel mechanisms with two virtual center-of-motion," *Mech. Mach. Theory* **181**, 105208 (2023).
- [35] J. Wang, C. Wu and X.-J. Liu, "Performance evaluation of parallel manipulators: Motion/force transmissibility and its index," *Mech. Mach. Theory* **45**(10), 1462–1476 (2010).
- [36] F. Xie, X.-J. Liu and J. Wang, "Performance evaluation of redundant parallel manipulators assimilating motion/force transmissibility," *Int. J. Adv. Robot. Syst.* **8**(5), 66 (2011).

- [37] X. Chen, X.-J. Liu, F. G. Xie and T. Sun, “A comparison study on motion/force transmissibility of two typical 3-DOF parallel manipulators: The sprint Z3 and A3 tool heads,” *Int. J. Adv. Robot. Syst.* **11**(1), 5 (2014).
- [38] C. Yang, W. Ye and Q. Li, “Review of the performance optimization of parallel manipulators,” *Mech. Mach. Theory* **170**, 104725 (2022).
- [39] X.-J. Liu and J. Wang, “A new methodology for optimal kinematic design of parallel mechanisms,” *Mech. Mach. Theory* **42**(9), 1210–1224 (2007).
- [40] Y. Lou, G. Liu, J. Xu, and Z. Li, “A general approach for optimal kinematic design of parallel manipulators,” **In: IEEE International Conference on Robotics and Automation, 2004 Proceedings ICRA'04 2004** (IEEE, 2004) pp. 3659–3664.
- [41] X.-J. Liu, J. Wang and G. Pritschow, “On the optimal kinematic design of the PRRRP 2-DoF parallel mechanism,” *Mech. Mach. Theory* **41**(9), 1111–1130 (2006).
- [42] Y. Lou, Y. Zhang, R. Huang, X. Chen and Z. Li, “Optimization algorithms for kinematically optimal design of parallel manipulators,” *IEEE Trans. Autom. Sci. Eng.* **11**(2), 574–584 (2013).